Omega Baryon Production as a Function of Multiplicity in Proton-Proton Collisions at $\sqrt{s} = 13$ TeV

Master's Thesis by Lisa Vergara

Supervised by David Silvermyr

& Peter Christiansen

August 13, 2019

LUND UNIVERSITY

Department of Physics

Division of Particle Physics

Abstract

In this thesis the production of the Ω^- and Ω^+ baryons, in proton-proton collisions at $\sqrt{s} = 13$ TeV, is analyzed as a function of charged-particle multiplicity. The events analyzed were recorded by the ALICE detector, at the LHC. The aim of the analysis is to study the QGP-signature of strangeness enhancement, in search for an enhancement of Ω^- and Ω^+ at high multiplicity collisions. The Ω^- (Ω^+) baryon is optimal for this study as it is a multi-strange baryon consisting of three strange (anti-strange) quarks. The analyzed events are separated according to their event multiplicity and the baryon candidates are reconstructed through the cascade decay topology, and identified through several selection criteria. The results show that there is a clear enhancement of Ω^- and Ω^+ production, compared to the charged-particle multiplicity, at high multiplicity events.

Populärvetenskaplig Sammanfattning

Som många kanske vet, är allting runtomkring oss (och även vi själva) uppbyggda av atomer. Atomer är dock inte de minsta byggstenarna som finns (se bild[1]), då de består av en kärna – som består av protoner och neutroner – och elektroner. Även protonerna och neutronerna består av partiklar, så kallade kvarkar, men där tar det stopp. De här kvarkarna (och även elektronerna) är vad som kallas elementarpartiklar och de består inte av andra partiklar – så vitt vi vet i alla fall. Partikelfysik handlar om just de här odelbara partiklarna och deras växelverkan, eller "samspel". Teorin som beskriver partikelfysik som bäst kallas för Standard Modellen och i den beskrivs även tre av de fyra fundamentala krafterna: den starka, elektromagnetiska och svaga kraften. Gravitationskraften är den fjärde fundamentala kraften, som inte beskrivs av Standard Modellen. Den elektromagnetiska kraften är kraften som håller ihop atomkärnor och elektroner i atomerna, medan den starka kraften håller ihop protoner och neutroner i kärnan, men även kvarkarna i protonerna/neutronerna.

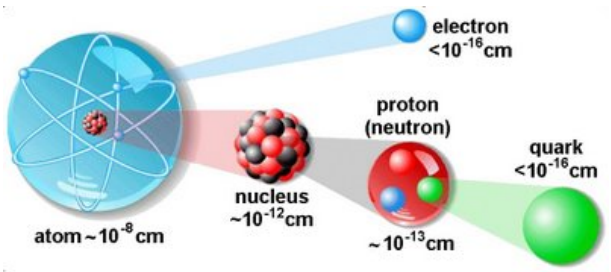

Kvarkar finns idag bara i bundna tillstånd (i t.ex. protoner/neutroner) och kan alltså inte studeras som fria partiklar, men cirka en miljondelssekund efter Big Bang var kvarkarna nästan fria i en soppliknande plasma kallad kvark-gluon plasman. Den här plasman kan idag skapas i världens största partikelaccelerator – LHC vid CERN i Schweiz – men bara i en bråkdelssekund. Vi kan alltså inte studera den här plasman under tiden den existerar, utan får studera signaturerna (i form av nya partiklar) som den lämnar efter sig.

I LHC kollideras bl.a. protoner med protoner (pp-kollisioner) och tunga bly-(atom)kärnor (som innehåller 164 protoner and 248 neutroner) med varandra (Pb-Pb kollisioner). Eftersom det behövs väldigt höga densiteter för att kvark-gluon plasman ska bildas, så är det i kollisioner med bly-kärnor som plasman bildas. Detta var i alla fall vad man trodde tills man hittade kvark-gluon plasma signaturer i vissa pp-kollisioner också. Man vet dock inte än om de här signaturerna kommer från kvark-gluon plasman eller om de har ett annat ursprung. I analysen som beskrivs i den här uppsatsen, studeras en av de här signaturerna i pp-kollisioner, genom att analysera produktionen av en s.k. baryon, en partikel som inte är en proton/neutron, men som också består av kvarkar. Detta görs så att man så småningom ska kunna ta reda på om det faktiskt bildas kvark-gluon plasma i pp-kollisioner också, eller om det är något annat som ger upphov till de kvark-gluon plasma-liknande signaturerna.

[1] Bild tagen från https://varldskrigenentreskolaneskilstuna.wordpress.com/faktabank/noteknik/kemifysik/

Contents

1 Introduction

Particle physics is the study of the fundamental constituents of matter and the interactions between them. Today, particle physics is best described by the Standard Model, a theory which is well confirmed by experimental observations. In the Standard Model, the different particle interactions are described by quantum field theories, and Quantum Chromodynamics (QCD) is the quantum field theory for the strong force – the force that binds quarks into hadrons (e.g. protons and neutrons) and hadrons into nuclei. The "force carrier" of the strong force is the gluon, a gauge boson which itself possesses the charge of the strong interaction, making it self-interacting. This characteristic of the gluon has two consequences, called color confinement and asymptotic freedom, which make the strong force between quarks behave in a similar way as a rubberband; the further apart quarks get, the stronger the force between them, making it impossible to separate quarks entirely and thus, to study them as free particles.

It is believed that approximately 10 μs after the Big Bang, there existed in our Universe a state of matter – called the Quark-Gluon Plasma (QGP) – where quarks and gluons were deconfined within a certain volume. Today, this plasma can be created in high-energy heavy-ion collisions, although, it exists only for $\sim 10^{-22}$ s, and it can therefore, not be observed directly. However, when the plasma is created in heavy-ion collisions, it leaves different signatures, by which its (previous) existence can be identified. One of these signatures is called strangeness enhancement, and it refers to the enhanced production of hadrons consisting of strange quarks.

It was previously thought that the Quark-Gluon Plasma could only be created in heavy-ion collisions and that smaller systems were not dense enough for the plasma to be created. These smaller systems, like proton-proton or proton-nucleus collisions, have therefore been used as a baseline for the standard QCD phenomena. However, several Quark-Gluon Plasma signatures have today been observed in high-multiplicity, small collisonal systems. The origin of these phenomena is still unknown, although, it is being investigated by both theoretical and experimental high-energy physicists, for instance within the CLASH project in Lund.

The aim of this thesis is to contribute to the study of the origin of the QGP-like signatures in proton-proton collisions, by analysing the production of the multi-strange Omega baryon, in search for an enhanced production at high multiplicities. The collisions analyzed in this thesis were recorded by the ALICE detector, at the LHC.

This thesis is organized as follows. The Standard Model of particle physics will be introduced in Chapter 1, while in Chapters 2 and 3 the ALICE detector and the Quark-Gluon Plasma will be presented. In Chapters 5 and 6, the analysis performed and the results obtained are described. Lastly, in Chapter 7, the conclusions drawn and an outlook are presented.

2 The Standard Model

The Standard Model (SM) is a mathematical theory, which today provides the best description of particle physics. It is a Quantum Field Theory (QFT) and thus, fully combines the realms of quantum mechanics and special relativity. The SM describes the properties of all the fundamental – or elementary – particles, which are particles with no (known) internal structure, by a set of quantum numbers (e.g. charge and mass); additionally, the SM describes the interactions of the particles, by the fundamental forces. [1, 2]

The particles of the SM are divided into two different categories, depending on their spin (i.e. internal angular momentum): fermions and bosons. The elementary fermions, which have half-integer spin, are known as the "matter" particles, while the elementary bosons, which have integer-spin, are known as the "force carriers", as they mediate the interactions (i.e. the fundamental forces) between the fermions. The Pauli exclusion principle – which states that two identical particles (two particles with the exact same quantum numbers) cannot, simultaneously, occupy the same quantum state – is obeyed by fermions, but not by bosons. [2, 3]

2.1 Particles & Forces of the Standard Model

The SM includes three of the four fundamental forces of nature: the strong, electromagnetic, and the weak force. The fourth fundamental force, which is not described by the SM, is the gravitational force. The three forces included in the SM are described by a QFT, in which the "matter" particles are treated as excitations of quantum fields that interact by the exchange of field quanta – the "force carriers". The "force carriers" are all spin-1 bosons and they are also known as the gauge bosons of the SM. [2, 4]

Table 1: The "force carriers" of the Standard Model

Boson	Force	Interacts with	Mass	Charge
Gluon (g)	Strong	Color charged particles	0	0
Photon (γ)	Electromagnetic	Electrically charged particles	0	0
$W^{\pm}$	Weak	Fermions	80.4 GeV	$\pm e$
Z^0	Weak	Fermions	91.2 GeV	0

The QFT for the strong force is called Quantum Chromodynamics (QCD) and it is associated with the massless gluon. The gluons couple to all particles which possess color charge, which is the charge of the strong force. The QFT for the electromagnetic force is called Quantum Electrodynamics (QED). This interaction is associated with the photon,

which is also massless and couples to all electrically charged particles, although, it is itself electrically neutral. The weakest force of the SM is the weak interaction; it is associated with the electrically charged W^+ and W^-, and with the electrically neutral Z^0. In Table 1 the gauge bosons of the SM are presented, together with the force they correspond to, the particles they couple to, their mass, and their electric charge in units of e (the magnitude of the electron's electric charge). [4]

The fermions of the SM are divided into quarks and leptons. There are six types – also called flavours – of both quarks and leptons, and these are arranged in three families – or generations – of doublets. Table 2 shows, together with their estimated bare masses, the six quarks of the SM: up, down, charm, strange, top, and bottom. As can be seen in the table, the masses of the quarks increase for each generation. The electric charge, which is given in the table in units of e, is $\frac{2}{3}$ and $-\frac{1}{3}$ for the quarks in the top and bottom row, respectively. Besides electric charge, quarks also posses color charge (the charge of the strong interaction); each quark flavor can, therefore, exist in three different colors. Further, quarks also posses a quantum number called baryon number B, which has so far been observed to be conserved. Each quark has $B = \frac{1}{3}$. [1, 2]

Table 2: The three generations of quarks of the Standard Model, together with their estimated bare masses. The electric charge of the particles is presented in units of e.

Quarks						
Charge	1st Generation		2nd Generation		3rd Generation	
$+\frac{2}{3}$e	Up (u)	2.3 MeV	Charm (c)	1.28 GeV	Top (t)	173 GeV
$-\frac{1}{3}$e	Down (d)	4.8 MeV	Strange (s)	95 MeV	Bottom (b)	4.18 GeV

Table 3 shows the six leptons of the SM: the electron, electron neutrino, muon, mu-neutrino, tauon, and tau-neutrino. The electric charge of the leptons is shown in units of e, being -1 for the leptons in the upper row, and 0 for the respective neutrinos. Although the charged leptons are shown together with their masses, which increase for each generation, no masses for the neutrinos are presented as they are not yet known. The leptons also posses a quantum number called lepton number L; the lepton number is defined per lepton family (e.g. e^- and ν_e have $L_e = 1$, while e^+ and $\bar{\nu}_e$ have $L_e = -1$) and has been experimentally observed to be conserved. [1, 2]

In addition to all the fermions mentioned, there exists for each one of them an antiparticle with the exact same mass, but opposite values of electric and color charge. In order to distinguish them from each other the particles and antiparticles are either denoted with their electric charge, or a bar is placed over the letter of the antiparticle. [1]

Table 3: The three generations of leptons of the Standard Model. Since the neutrino masses are not yet known, only the masses of the leptons in the upper row are given. The electric charge of the particles is presented in units of e.

Leptons							
Charge	1st Generation		2nd Generation		3rd Generation		
-e	Electron (e)	0.5 MeV	Muon (μ)	106 MeV	Tau (τ)	1.78 GeV	
0	e-neutrino (ν_e)	? eV	μ-neutrino (ν_μ)	? eV	τ-neutrino (ν_τ)	? eV	

The last particle needed, in order for the SM to be complete, is called the Higgs boson. The particles of the SM acquire their mass through their interaction with the Higgs field, while the Higgs boson is (in consistency with QFT) an excitation of the Higgs field. The Higgs boson is a spin-0 scalar boson, whose descovery in 2012 led to the completion of the SM. [1, 4]

2.2 Quantum Chromodynamics

Quantum Chromodynamics (QCD) is the quantum field theory describing the strong force within the Standard Model. As was previously mentioned, the gluons are the gauge bosons of the strong force and they couple to color charge, which both the quarks – and the gluons themselves – possess. Quarks can exist in three different colors: red (r), green (g) or blue (b), or three respective anticolors ($\bar{r}, \bar{g}, \bar{b}$). The gluons, however, can exist in eight different color states; these states are linear combinations of the mentioned color and anticolor charges. The fact that gluons themselves posses color charge leads to a self-interaction of the gluon, which has two further consequences: color confinement and asymptotic freedom. [4, 5]

2.2.1 Color Confinement & Asymptotic Freedom

Color confinement is a hypothesis which explains why no free quarks have ever been observed. It states that colored particles are confined to be within color neutral bound states and that they, therefore, cannot propagate as free particles. Qualitatively, when two free quarks are pulled apart, they interact by exchanging virtual gluons – which also interact with each other due to them both possessing color charge. This interaction creates an attractive potential, which grows linearly with the distance between the quarks. Consequently, the energy needed to entirely separate the quarks would be infinite [4]. It is for this reason that quarks and gluons – which are collectively called partons – are confined within their bound states, called hadrons. There exists two types of hadrons: the baryons and the mesons. The baryons consist of three quarks (qqq), one of each color, while the mesons consist of a quark-antiquark pair ($q\bar{q}$) [2].

When the distance between the partons becomes very small, or equally the momentum transfer very large, color confinement no longer applies, and instead, asymptotic freedom starts to prevail. Asymptotic freedom is when the interaction between the partons gets weak enough and the partons behave as nearly free. In simple terms, the effect of asymptotic freedom can be explained by considering a (for example) blue quark at the origin, for which the process $q_b \rightarrow q_r + g_{b\bar{r}}$ is possible. The gluon, which now carries the blue color charge, is not concentrated at the origin, and the charge is instead smeared out in a gluon cloud. Thus, if a probe gets close to the origin it would no longer see a blue quark. This process is called antiscreening and its effect becomes larger with higher momentum transfer, as the probability of radiation also increases, less color charge is concentrated at the origin and the interaction becomes weaker. [1]

3 Experiment

CERN (the European Organisation for Nuclear Research) hosts the largest and most powerful particle accelerator ever built – the Large Hadron Collider (LHC). The LHC is located approximately 100 m underground near Geneva, Switzerland, and it has a circumference of 27 km. Inside the accelerator two particle beams, travelling in opposite directions and at nearly the speed of light, are collided at four different intersection points; detectors are located at each one of these points: the ATLAS, ALICE, CMS, and LHCb detectors. Before colliding, the two beams travel in separate beam pipes, which are kept at ultrahigh vacuum. Superconducting electromagnets are chilled to $-271.3°$C in order to provide strong electromagnetic fields which accelerate and bend the beams around the accelerator ring. [6, 7]

At the LHC, three different types of collisions occur: proton-proton (pp), lead-lead (Pb-Pb) and proton-lead (p-Pb). Today, energies of $\sqrt{s} = 13$ TeV and $\sqrt{s_{\mathrm{NN}}} = 5.02$ TeV have been achieved for pp and Pb-Pb collisions, respectively. [6, 8]

3.1 The ALICE Detector

ALICE (A Large Ion Collider Experiment) is placed at P2, one of the four intersection points where particles are made to collide, at the LHC. The detector is located ~ 56 m underground and weighs 10,000 tonnes; it is 16 m high, 16 m wide, and 26 m long, and it is designed to handle the very high particle densities created in central Pb-Pb collisions [9]. The ALICE detector coordinate system has its origin, $(x, y, z) = (0, 0, 0)$, at the center of the detector, at the beams interaction point. The beam direction is defined as the z-axis, while the x-axis is horizontally perpendicular to the beam direction and pointing to the center of the accelerator. The +y-axis points upward and is, thus, perpendicular to the x,z-plane. The azimuthal φ and polar θ angles increase from $x\,(\varphi = 0)$ to $y\,(\varphi = \pi/2)$ and from $z\,(\theta = 0)$ to the x,y-plane $(\theta = \pi/2)$, respectively [10].

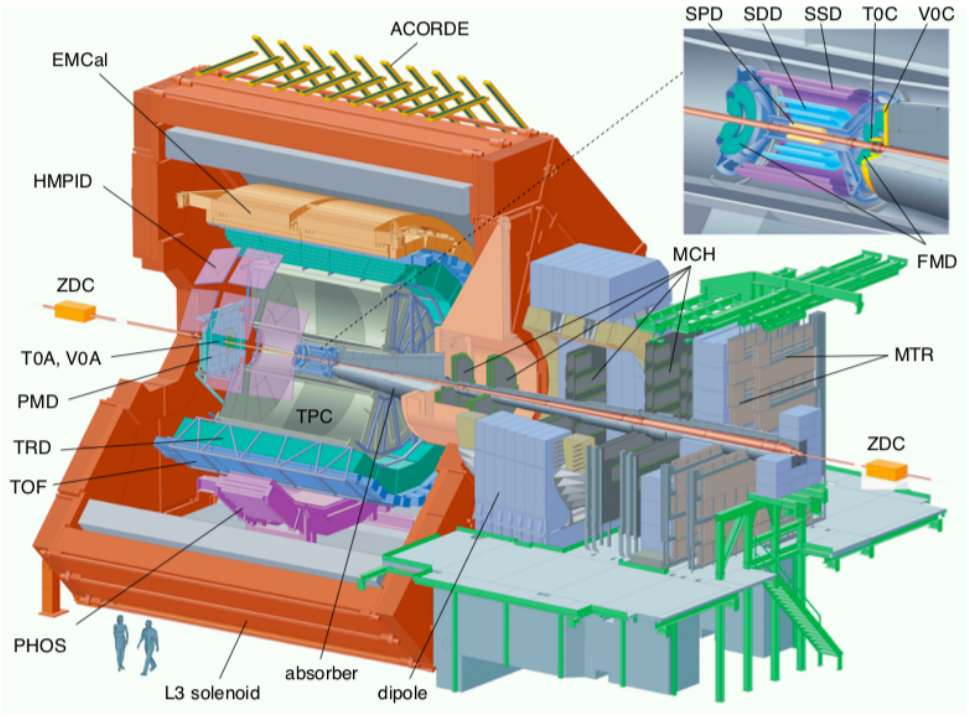

Figure 1: A schematic illustration of the ALICE detector with all the subdetectors, which are divided into the categories central-barrel detectors, forward detectors, and the MUON spectrometer [11].

ALICE consists of 17 subdetectors, which are divided into three categories: central-barrel detectors, forward detectors, and the MUON spectrometer. A schematic illustration of the ALICE detector is shown in figure 1. The central-barrel detectors comprise the Inner Tracking System (ITS), Time Projection Chamber (TPC), Transition Radiation Detector (TRD), Time Of Flight (TOF), Photon Spectrometer (PHOS), Electromagnetic Calorimeter (EMCal), and High Momentum Particle Identification Detector (HMPID); these are surrounded by the L3 solenoid magnet. The principle charged-particle tracking detectors in ALICE are the TPC and the ITS, these will be described further in sections 3.1.1 and 3.1.2, respectively. The TRD detector is also used for the tracking of charged particles, as well as electron identification. The TOF is used for charged particle identification; it measures the time of flight of the particles over a certain distance and thus determines their velocities. The ITS, TPC, TRD and TOF cover the full azimuth at midrapidity ($|\eta| \lesssim 0.9$). The high-resolution PHOS and the large-acceptance EMCal are both calorimeters which measure the energies of the particles, especially of photons and electrons. Lastly, the HMPID detector is a Cherenkov detector used for the identification of charged hadrons. [9, 11]

The forward detectors include the Photon Multiplicity Detector (PMD), Forward Multiplicity Detector (FMD), T0 detector, V0 (or VZERO) detector, and Zero Degree Calorimeter (ZDC). The PMD and the FMD detectors both measure the multiplicity; additionally, the PMD also measures the spatial distribution of photons and the FMD

measures the orientation, in the vertical plane, of a collision. The T0 detector measures the time and the longitudinal position of a collision. The V0 detector, which will be described further in section 3.1.3, and the ZDC detector measure the collision centrality. [9, 11]

The MUON spectrometer is designed for the detection of heavy-quark resonances, through their decay to $\mu^+\mu^-$. The muons are detected by the Muon Tracking Chambers (MCH), which are located before and after the Muon Magnet – by which the trajectories of muons with high momentum are bent. Finally, the passage of the muons is signaled by the Muon Trigger (MTR), while other particles (e.g. hadrons) are stopped by the large amount of material in the spectrometer. [9, 11]

3.1.1 The Time Projection Chamber

The main tracking detector in ALICE is the TPC, which covers the entire azimuthal range and the central pseudorapidity range of $\eta < 0.9$. The TPC is a large cylinder filled with gas; it has an inner radius of ∼85 cm, an outer radius of ∼250 cm, and a drift volume of 90 m^3 filled with Ne-CO_2 [11, 12]. An illustration of the TPC is shown in figure 2.

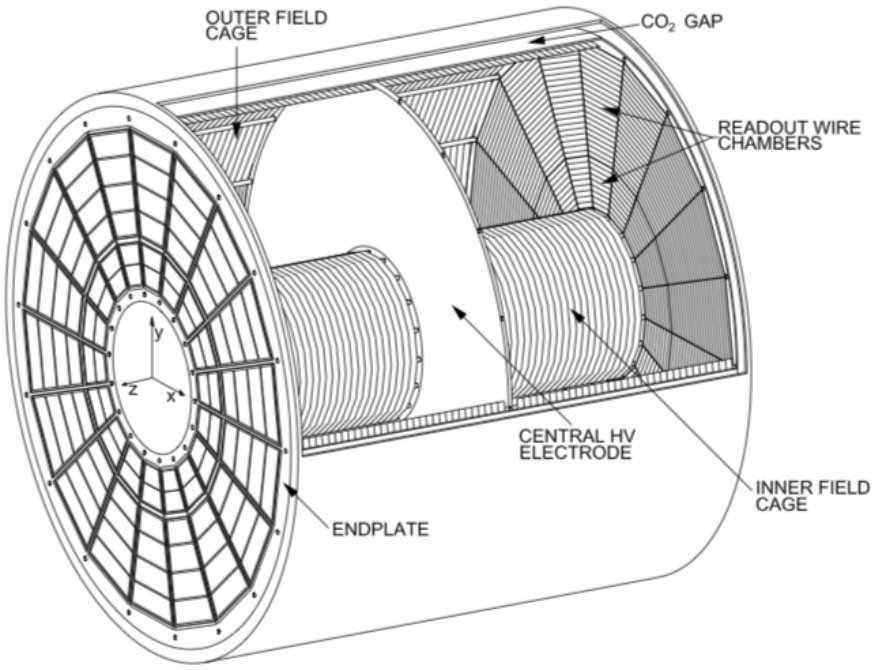

Figure 2: A schematic illustration of the Time Projection Chamber, the main tracking detector of the ALICE detector. Figure taken from [13].

The length of the TPC along the z-direction is 500 cm, although it is divided in two parts by the central electrode. When charged particles are created in a collision they traverse the TPC, ioninizing the gas and liberating electrons which then drift, due to

the uniform electric field defined by the field cage, towards the end plates. The end plates are equipped with Multi-Wire Proportional Chambers (MWPC), which provide information about the momentum, and about the trajectory of the particles in three-dimensions [12, 14]. The TPC is currently undergoing an upgrade, where the MWPC will be replaced by Gas-Electron Multiplier (GEM) technology, to cope with larger interaction rates.

Besides tracking, the TPC also measures the specific ionization energy loss of particles per distance unit ($\mathrm{d}E/\mathrm{d}x$) – i.e. the energy the particles loose, while passing through the detector – and thus, provides particle identification. The identification of the particles is possible by measuring the specific energy loss, the charge, and the momentum of the particle, simultaneously [11]. The energy loss of a particle – of mass m, charge z, and velocity v – is given by the Bethe-Bloch formula:

$$\left\langle \frac{\mathrm{d}E}{\mathrm{d}x} \right\rangle = \frac{4\pi N e^4}{m_e c^2} \frac{z^2}{\beta^2} \left(\ln \frac{2mc^2\beta^2\gamma^2}{I^2} - \beta^2 - \frac{\delta(\beta)}{2} \right), \tag{1}$$

where N is the electron density of the material, e is the elementary charge, m_e is the mass of the electron, I is the mean excitation potential of the material, $\beta = v/c$, and $\gamma = 1/\sqrt{1-\beta^2}$. The different particle species will, depending on their mass and charge, cluster in different bands [15]. The energy loss per distance unit, as a function of momentum as measured by the TPC in Pb-Pb collisions is shown in figure 3, where the bands of the different particle species can clearly be seen.

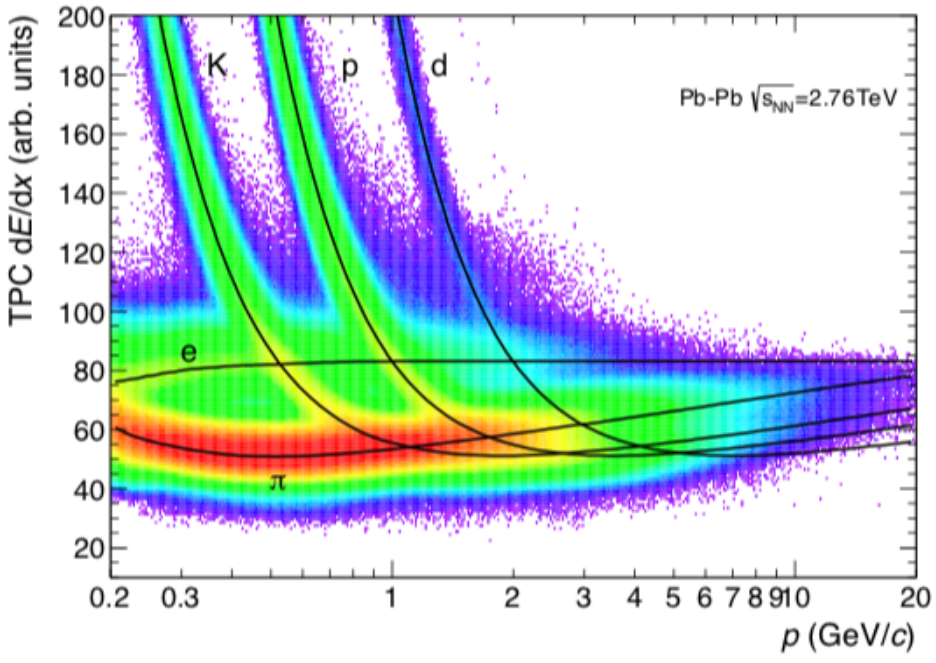

Figure 3: The specific energy loss per distance unit, $\mathrm{d}E/\mathrm{d}x$, as a function of the momentum, measured by the TPC in Pb-Pb collisions at $\sqrt{s_{NN}} = 2.76$ TeV. The histogram is taken from reference [11].

3.1.2 The Inner Tracking System

The ITS is composed of six cylindrical layers of silicon tracking detectors: two Silicon Pixel Detectors (SPD), two Silicon Drift Detectors (SDD), and two Silicon Strip Detectors (SSD). It surrounds the beam pipe and its innermost layer is located at a radius of 4 cm away from it, which is the smallest radius allowed, while its outermost layer is at a radius of 43 cm away. The ITS detector covers the entire azimuthal range and the central pseudorapidity range of $\eta < 0.9$ [11, 12]. The ITS is, as the TPC, undergoing a major upgrade during 2019-2020.

Two of the main purposes of the ITS are to reconstruct the primary and secondary vertices, which are determined by the two SPD detectors, and to identify charged particles with low p_T with the four outermost layers. The SDD and SSD detectors provide a measurement of the ionization energy loss per distance unit $\mathrm{d}E/\mathrm{d}x$. [11, 12]

3.1.3 The V0 Detector

The V0 detector consists of two circular arrays of 32 plastic scintillator counters each: the V0A and V0C. These are located on either side of the ALICE interaction point; the V0A is at a distance of 340 cm and the V0C is at a distance of 90 cm from the nominal interaction point. The V0 covers small angles, as the pseudorapidity range covered by the V0A is $2.8 < \eta < 5.1$ and the range covered by the V0C is $-3.7 < \eta < -1.7$. [11, 12]

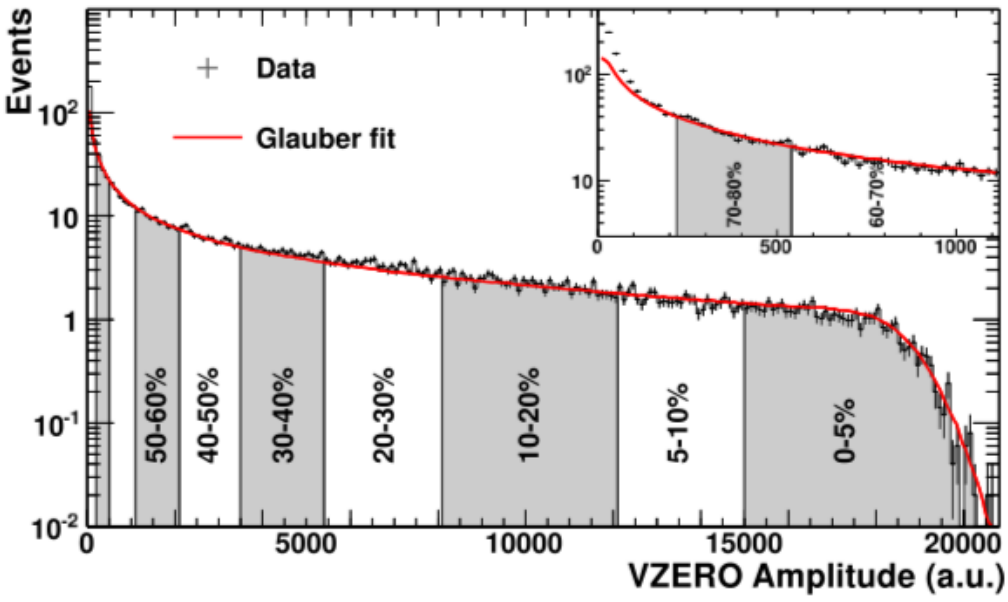

Figure 4: The V0 (or VZERO) amplitude distribution, fitted with a Glauber model (red line), from Pb-Pb collisions at $\sqrt{s_{NN}} = 2.76$ TeV. The low percentages correspond to a high collision multiplicity, while the high perentages correspond to lower collision multiplicities. [16]

The V0 detector has various functions. One of the main purposes is to provide the basic (level 0) trigger in ALICE, called the minimum bias trigger. By measuring the energy deposited in the detector, the V0 also measures the charged particle multiplicity, which in turn provides a collision centrality estimation, by integration of the multiplicity amplitude distribution. In figure 4, a distribution of the V0 multiplicity amplitude, which is a sum of the V0A and V0C amplitudes, is shown. The distribution is fitted by a Glauber Model (red line), which describes the geometry of the collision. The more central a collision is, the higher the multiplicity and the V0 amplitude. [11, 12]

3.2 Collision Variables

When particles are collided at the LHC, new particles are created and detected. In order to understand what happens in the collisions, variables which describe the particles have to be defined. Furthermore, since the particles travel at relativistic velocities, classical mechanics has to be extended in order to be compatible with the theory of special relativity. The variables presented in this section are defined with respect to the ALICE detector coordinate system, described at the beginning of section 3.1.

3.2.1 Transverse Momentum

A useful variable, that is widely used in high-energy physics, is the transverse momentum p_T:

$$p_T = \sqrt{p_x^2 + p_y^2}, \tag{2}$$

which is the momentum component in the transverse, or xy, plane. Thus, in equation 2, p_x and p_y are the momentum components along the x- and y-direction, respectively. The transverse momentum, together with the azimuthal angle, yield the cartesian momentum-components, by:

$$p_x = p_T \cos\varphi \tag{3}$$

$$p_y = p_T \sin\varphi \tag{4}$$

$$p_z = \sqrt{|\mathbf{p}|^2 - p_T^2} \tag{5}$$

where p_z is the momentum component along the beam-direction and $\mathbf{p} = (p_x, p_y, p_z)$ is the three-momentum vector. [8]

3.2.2 Invariant Mass & Center-of-Mass Energy

In a relativistic context a particle, of mass m and velocity vector $\mathbf{v}$, can be characterized by its four-momentum $p^\mu = (E,\ \mathbf{p})$, where $E = \gamma mc^2$ is the relativistic energy, and $\mathbf{p} = \gamma m\mathbf{v}$ is the relativistic momentum of the particle; $\gamma = 1/\sqrt{1 - v^2/c^2}$ is the Lorentz factor. The scalar product of the four-momentum, in natural units ($c = 1$), is given by

$$p^\mu p_\mu = E^2 - \mathbf{p}^2 \tag{6}$$

This scalar product is a Lorentz invariant quantity, which means it is unaffected by Lorentz transformations and is thus, the same in all reference frames. [4]

Two particles of equal mass and energies, traveling in opposite directions at the LHC, can be described by their four-momenta $p_1 = (E, \mathbf{p})$ and $p_2 = (E, \text{-}\mathbf{p})$. Since both energy and momentum are conserved, the energy available to create new particles when the original particles collide, can be calculated by:

$$p^\mu p_\mu = \left(\sum_{i=1}^{n} E_i\right)^2 - \left(\sum_{i=1}^{n} \mathbf{p}_i\right)^2 . \tag{7}$$

Inserting the energy and momenta of the particles in this equation gives:

$$p^\mu p_\mu = (E + E)^2 - (\mathbf{p} + (-\mathbf{p}))^2 = E^2 + 2E^2 + E^2 = 4E^2 \equiv s \tag{8}$$

where $\sqrt{s}$ is Lorentz invariant and is called the center-of-mass energy. [4, 17]

For a particle at rest ($p^\mu = (mc^2, 0)$), the scalar product of the four-momentum yields

$$p^\mu p_\mu = E^2 - \mathbf{p}^2 = m^2 \tag{9}$$

where m is the rest mass of the particle. This quantity is also Lorentz invariant and it is, therefore, also called the invariant mass. When particles created in the collisions decay before reaching the detectors where they can be identified, their invariant mass can be calculated through their decay products and equation 7, where E_i and $\mathbf{p}_i$ are the energy and momentum of the decaying particle's n decay products. [4]

3.2.3 Rapidity & Pseudorapidity

A quantity that is convenient to use as a measure of relativistic velocity in high-energy collisions is the rapidity y, defined as

$$y = \frac{1}{2} \ln \left(\frac{E + p_z}{E - p_z} \right) . \tag{10}$$

Although not invariant under Lorentz transformations, the rapidity is additive under boosts in the beam direction. These boosts are created, since the center-of-mass of the particles accelerated is moving relative to the beam axis. The rapidity takes values between $-\infty < y < \infty$, where a particle traveling along the z-axis would have a rapidity of $y \to \infty$ and a particle scattered at 90° from the beam axis would have $y = 0$. [5, 18]

Calculating the rapidity is not always possible, since both the energy and the z-component of the momentum are needed. However, at very high energies, the mass of the particles can be neglected since $\mathbf{p} \gg m$ and thus, $E \approx \mathbf{p}$. This yields a new variable, called the pseudorapidity η, defined as

$$\eta = \frac{1}{2} \ln \left(\frac{|\mathbf{p}| + p_z}{|\mathbf{p}| - p_z} \right) = - \ln \tan \left(\frac{\theta}{2} \right) \tag{11}$$

where θ is the polar angle, which increases from the z-axis to the transverse (x,y)-plane. At very high energies $\eta \approx y$. In figure 5 different values of pseudorapidity are shown with respect to the polar angle. Along the z-axis, $\theta = 0°$ and $\eta \to \infty$, and when $\theta = 90°$, $\eta = 0$. [5, 18]

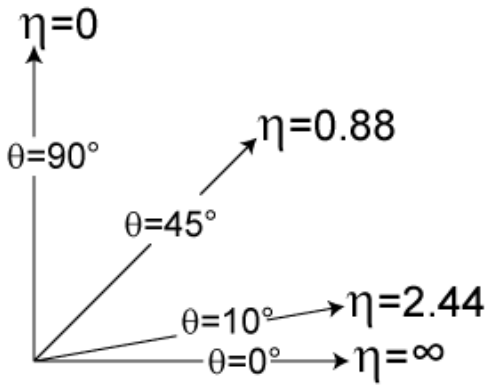

Figure 5: Different values of pseudorapidity with respect to the polar angle θ. The polar angle $\theta = 0$ along the beam-axis. Figure taken from [19].

3.2.4 Collision Centrality & Multiplicity

Heavy ion collisions can be separated according to their collision centrality. Heavy ions are extended objects, which can collide head on (in a central collision), but also peripherally. How central a collision is cannot be measured directly, and thus, other observables have to be used in order to determine the centrality of a collision. The charged particle multiplicity, often simply referred to as the multiplicity, measures the charged particle production in a collision and is related to the centrality estimate of a collision. Central collisions yield high event multiplicty, while peripheral collisions yield low event multiplicities [5].

4 The Quark-Gluon Plasma

At ordinary energies, densities, and temperatures partons are, as already mentioned, confined within hadrons. At (extremely) high energies, densities, and temperatures, however, there can occur a phase transition to a state of matter where the partons become deconfined and where they can move as free particles across a certain volume. This state of matter is called the Quark-Gluon Plasma (QGP) [2]. It has been calculated that the QGP is created after a critical energy density of ~ 1 GeV fm^{-3}, or a critical temperature of ~ 200 MeV, is reached. It is believed that the QGP existed in the Universe approximately 10 μs after the Big Bang and it is believed to exist at the core of neutron stars. Today, the QGP can also be created in heavy ion collisions in high-energy particle accelerators [5, 20].

4.1 QGP in Heavy Ion Collisions

A QGP system undergoes different phases when produced in relativistic heavy ion collisions: pre-equilibrium stage, expansion stage, and freeze-out. At the pre-equilibrium stage the partonic collisions, which take place when heavy ions are collided at relativistic energies, produce a fireball (the QGP). The fireball is initially not in equilibrium, but a local equilibrium state is established through frequent collisions of the partons, which are the constituents of the fireball. At the expansion stage the partons are deconfined in the fireball, which will undergo a collective, or hydrodynamic, expansion due to a thermal pressure acting against the surroundings. This expansion will decrease the density of the system, causing it to cool down. When the temperature of the system is less than the critical temperature (mentioned above) the partons will hadronize – i.e. form hadrons in which they will be confined. The freeze-out stage is divided into two parts. The first is the "chemical" freeze-out, in which local equilibrium is maintained due to colliding hadrons, and the system expands and cools further. Eventually, the inelastic collision rate will be too small in comparison to the expansion rate and the hadron abundances will be fixed. The elastic collisions, on the other hand, will maintain the local equilibrium, allowing the system to keep expanding and cooling. When the distance between the hadrons becomes larger than the range of the strong interaction, the local equilibrium will no longer be maintained (due to the low rate of collisions). This is the final "kinetic" freeze-out, from which the hadrons will propagate towards the detectors. [5]

When the QGP is created in relativistic heavy ion collisions, the stages described above do not last for long; in fact, the partons hadronize after only $\sim 10^{-22}$ s [20]. For this reason, the QGP cannot be directly observed, and information about the QGP has to be extracted from detected final-state particles, i.e. the hadrons measured by the detectors after the kinetic freeze-out stage. If produced in the collisions, the QGP will "leave signatures" which are reflected in the final state particles. There are many such signatures of the QGP; one of them is called strangeness enhancement and it will be described below [5].

4.1.1 Strangeness Enhancement

Strangeness enhancement refers to an enhanced production of strange quarks, which manifests itself as an enhanced production of strange (or multi-strange) hadrons. Strange (or multi-strange) hadrons are hadrons consisting of one (or more) strange quarks. Strangeness enhancement in heavy ion collisions, relative to smaller collision systems (involving protons), was one of the predicted QGP signatures. The enhancement is more distinct for multi-strange hadrons, than for single-strange hadrons. [21]

The strange quark is not present in the initial state (or collided) particles, thus, it is known that the strange quarks are produced in the collision. The production occurs in the processes $q + \bar{q} \rightarrow s + \bar{s}$ and $g + g \rightarrow s + \bar{s}$, although, the large number of gluons in the plasma makes the gluon fusion dominate the production process. After the strange quarks are created they will combine with other non-strange quarks – and with each

other – in the hadronization stage, yielding the production of strange and multi-strange hadrons. [5]

4.2 QGP Features in Small Collisional Systems

As was already mentioned, the Quark Gluon Plasma can today be created in relativistic heavy ion collisions, known as large collisional systems. Small collisional systems (e.g. p-Pb or pp) were believed to be too small (not dense enough) for the QGP to be created and were therefore used as a baseline for the standard QCD phenomena. However, several QGP-signatures have today been observed in high-multiplicity, small collision systems – one of them being strangeness enhancement [22]. The origin of these QGP-like signatures is still unknown, although, it is being investigated in the CLASH project in Lund, where both theoretical and experimental high-energy physicists are involved.

The article in reference [22] presents the first observation of strangeness enhancement in high-multiplicity proton-proton collisions.

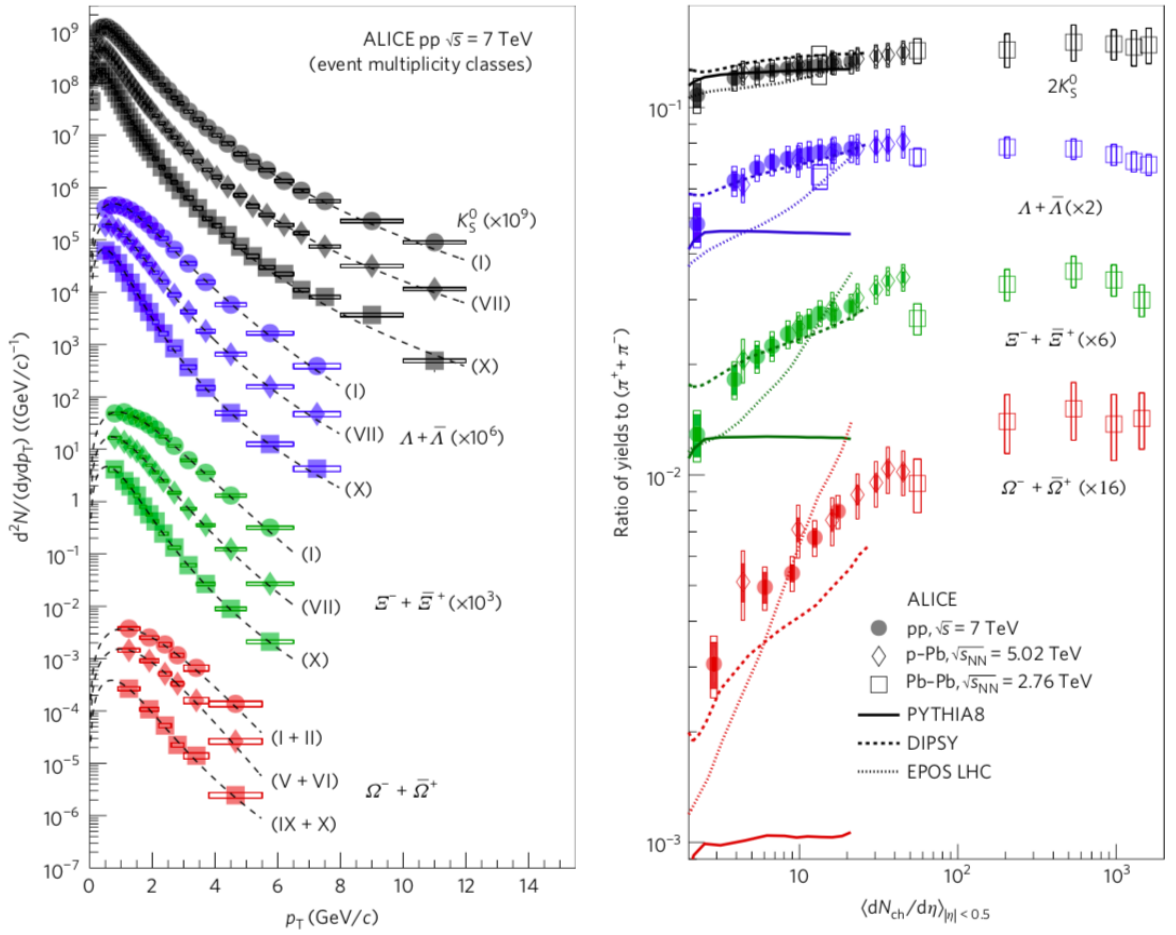

(a) p_T spectra of strange hadrons.

(b) Ratio of yields to pion yield, vs. $\mathrm{d}N_{\mathrm{ch}}/\mathrm{d}\eta$.

Figure 6: Results from reference [22], showing the first observations of strangeness enhancement in high multiplicity pp-collisions.

The measurements were performed at a center-of-mass energy of 7 TeV and at midrapidity $|y| < 0.5$, with the ALICE detector at the LHC. In figure 6a the p_T-spectra showing the multiplicity dependence of the production of particles with different amount of strangeness ($\Omega^- + \Omega^+$, $\Xi^- + \Xi^+$, $\Lambda + \bar{\Lambda}$, and K^0_s) is shown, where the higher the multiplicity, the higher the number of hadrons produced. Figure 6b shows the ratio of the yields of the strange hadrons to the pion ($\pi^+ + \pi^-$) yield as a function of the charged-particle multiplicity density ($\mathrm{d}N_{\mathrm{ch}}/\mathrm{d}\eta$). The results are compared to p-Pb and Pb-Pb results at the LHC. In the figure it can clearly be seen how the production of the hadrons increases with increasing $\mathrm{d}N_{\mathrm{ch}}/\mathrm{d}\eta$, and that this increase is much more pronounced the more strange quarks the hadron is composed of. In the high-multiplicty events, the results of the study approach the results obtained from systems where the QGP is formed. Furthermore, similar measurements have been performed by ALICE in p-Pb collisions at a center-of-mass energy of 5.02 TeV, and the results are in accordance with each other, suggesting that the final state system created in high-multiplicity collisions is responsible for the phenomena. The analysis presented in this thesis is similar to the analysis in [22], although it focuses only on the multi-strange Ω baryon, and it is done at a higher center-of-mass energy and up to higher p_T values.

5 Analysis

The data analysis described in this thesis was performed with the AliRoot framework, which is based on the ROOT software [23]. ROOT is an object-oriented framework, which uses C++ as an implementation language; it was created at CERN for storing and analysing data [24]. AliRoot is the framework – for analysis and simulation – which was designed for the ALICE detector [23].

5.1 Experimental and Simulated Data Samples

To obtain the results in this analysis, data recorded by the ALICE detector in 2016 (in the period LHC16k) was analyzed. This experimental data sample contains approximately $125 \cdot 10^6$ pp collisions, or events, at $\sqrt{s} = 13$ TeV.

In addition to the experimental data sample, a Monte Carlo (MC) simulated data sample, containing approximately $37.5{\cdot}10^6$ events, was analyzed. Monte Carlo simulations use the generation of random numbers to create simulated data, which behaves and fluctuates (on average) as real data. In the MC data the pp collisions, and the particles produced in it, were generated by the program PYTHIA, which is a general purpose event generator. This simulation of generated particles was combined with a detector simulation done with the program GEANT3. With GEANT3 the particles' passage through the detectors and their interactions with matter are simulated, after which the same event reconstruction and analysis as in real data can be applied. The difference between experimental and simulated data is that in the simulated data the "correct

solutions" are available. For that reason, all the particles created in the simulation have a (PDG-) code, which can be used to select the particles wanted in the analysis. [25, 26]

The simulated data of the generated particles, without the detector simulation, will in this analysis be referred to as MC_{gen}, while the simulated data of the generated particles after the detector simulation and reconstruction will be called MC_{rec}. The MC_{rec} is divided into $\mathrm{MC}_{rec}^{blind}$ and MC_{rec}^{PDG}, where "*blind*" stands for an analysis performed exactly as with experimental data, while "PDG" is an analysis performed by using the known "correct solutions".

5.2 The Ω^- Baryon

The Ω^-, and its antiparticle Ω^+, are multi-strange baryons composed of three strange (sss) quarks, and three anti-strange ($\bar{s}\bar{s}\bar{s}$) quarks, respectively. The Ω^- has an electric charge of -1e, while its anti-particle has a positive electric charge of +1e; they both have a mass of 1672.45 ± 0.29 MeV/c^2 . These Ω particles decay weakly and have a mean lifetime (τ) of $(0.821 \pm 0.011) \cdot 10^{-10}$ s, which corresponds to a decay length ($c\tau$) of 2.461 cm, and means a decay of the particles before reaching the main tracking detectors, when created in a collision. The main decay channels for these Ω baryons, with a branching ratio of $(67.8 \pm 0.7)\%$, are:

$$\Omega^- \to \Lambda + K^- \to (p + \pi^-) + K^- \tag{12}$$

$$\Omega^+ \to \bar{\Lambda} + K^+ \to (\bar{p} + \pi^+) + K^+, \tag{13}$$

where the Λ ($\bar{\Lambda}$) decays further and mainly (with a branching ratio of $(63.9 \pm 0.5)\%$) to a $p(\bar{p})$ and a $\pi^-(\pi^+)$. The electrically neutral $\Lambda(\bar{\Lambda})$ has a mean lifetime of $(2.632 \pm 0.020) \cdot 10^{-10}$ s, a corresponding decay length of 7.89 cm, and does also decay weakly before reaching the end of the detectors. Conversely, the $K^-(K^+)$, $\pi^-(\pi^+)$, as well as the stable $p(\bar{p})$ live for long enough time to reach the detectors [27]. From hereon, all the mentioned particles will be denoted without their electric charge and antiparticle-bar when both the particle and antiparticle are being referred to.

5.2.1 The Cascade Decay Topology

In high-energy particle collisions Ω baryons are created at the interaction point, or primary vertex (PV); they then travel a short distance before decaying, as in equation 12 and 13, at the secondary vertex (SV). Unlike the K meson, which reaches the detectors where it can be identified, the Λ baryon decays at the tertiary vertex (TV). This decay appears as a reconstructed V-shaped structure in the detectors due to the electrically charged decay products and is called a V^0 decay topology. The decaying particle (the Λ) is called the V^0 particle; the zero refers to the electrical neutrality of the particle. As the decay of the Ω particle is a two-step process, where one of the daughters is a V^0 particle which decays further, its decay topology is called a cascade. The charged meson K^- to

which the Ω also decays is called a bachelor. The cascade decay topology of the Ω^- is shown in figure 7. [21, 28]

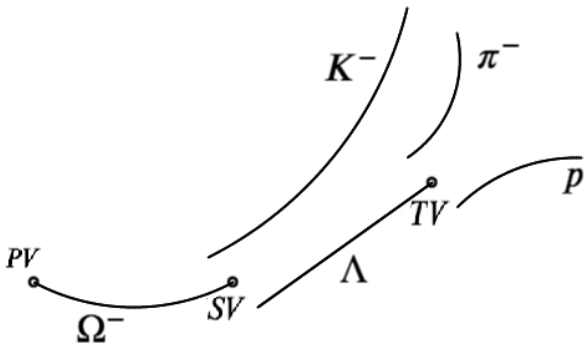

Figure 7: The cascade decay topology.

5.3 Selection criteria

The number of events that the experimental and simulated data samples contained was given in section 5.1. Although, a subset of these events was analyzed, since an event selection was performed in order to analyze only the "good" events. In order for the event to be analyzed it had to:

1. have a reconstructed primary vertex (within 10 cm of the center of the detector),
2. and not be a pile-up event.

The first criteria demands the event to have a reconstructed primary vertex, no further than 10 cm away, along the z-axis, from the nominal interaction point (the center of the detector). This reduces background events and minimizes the number of reconstructed tracks outside of the ALICE central barrel acceptance. Pile-up events are events containing more than one collision; these were also removed. After the event selection, the number of events (N_{ev}) in the experimental data set was approximately $119.55 \cdot 10^6$, while the number of events ($N_{\text{ev}}^{\text{MC}}$) in the simulated data set was approximately $36 \cdot 10^6$.

5.3.1 Selection of Ω Candidates

As was previously mentioned, the Ω baryon does not live for long enough time to reach the detectors, and so the detectable decay products have to be used in order to identify the Ω:s produced in the collisions. Candidates for the detectable decay products of Λ, namely p and π, were therefore identified first – in order to reconstruct the Λ candidates – and then candidates for the K meson were identified – in order to reconstruct the Ω candidates. At the analysis level, this is done by applying cuts – or selection criteria – in order to discard tracks from the wrong particles, or from wrong combinations. The cuts

applied in this analysis are obtained from the preliminary analysis in reference [28] and the values for each cut are given in Table 4.

The cuts applied for the p, π and K were:

- **Pseudorapidity (η):** the cut on pseudorapidity is applied in order to reject the tracks which do not have full detector acceptance; pseudorapidity was explained in section 3.2.3.

- **TPC PID (N_σ):** in figure 3 the particle energy loss per distance unit was shown as a function of the momentum measured by the TPC. With the TPC PID cut one of the particle bands ($p/\pi/K$) and a certain number of σ around this band are chosen, this way the p, π and K are identified and the background is minimized.

- **Distance of closest approach between one daughter particle and the primary vertex ($DCA_{\text{Bachelor-PV}}$, $DCA_{V^0\text{daughters-PV}}$):** this is the shortest distance between the primary vertex and the extended track of a daughter particle. This cut is applied in order to avoid mistaking a daughter particle with a particle coming from the primary vertex, thus this DCA must be larger than a certain value. The $DCA_{\text{Bachelor-PV}}$ is illustrated in figure 8.

For the reconstructed particles (Ω and Λ), the cuts applied were:

- **Distance of closest approach between daughters ($DCA_{\text{Bachelor-}V^0}$, $DCA_{V^0\text{daughters}}$):** this is the shortest distance between two daughter particles. This cut is applied to increase the probability that the two daughter particles are from the same mother; the distance between the daughters must, thus, be smaller than a certain value. These cuts are both illustrated in figure 8.

- **Transverse decay radius (r_{dec}):** This cut is applied to ensure that the different vertices can be separated. If the particles decay too close to where they were created, it might be difficult to separate the vertices, thus the distance between two vertices in the transverse plane has to be larger than a certain value. Since the decay length of Ω is shorter than that of the Λ, $r_{dec}(\text{cascade}) < r_{dec}(V^0)$.

- **Cosine of Pointing Angle (cos(PA)):** the pointing angle is the angle between the particle's momentum (which is the sum of its daughters' momenta) and a vector which connects the primary vertex with the vertex where the particle decays (SV for the cascade particle, TV for the V^0 particle). In the optimal case, the pointing angle is 0; for this analysis the $\cos(\text{PA}) < 0.97$, where 0.97 corresponds to a PA of $\sim 14°$. The cos(PA) for the Ω^- is illustrated in figure 8.

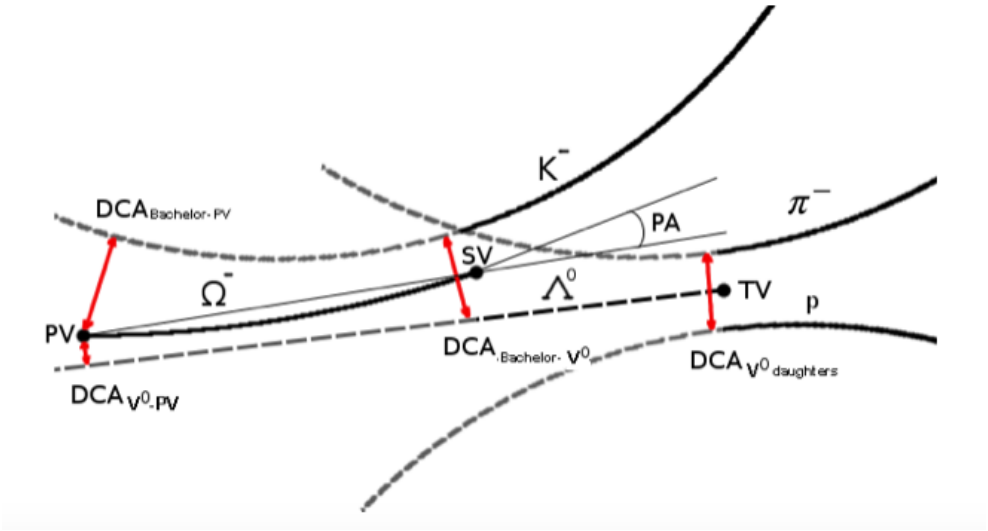

Figure 8: Illustration of the cascade decay topology together with several of the cuts applied in this analysis. The figure is taken from reference [29].

Besides these track-level cuts, there were three additional cuts applied. Two of these three cuts were constraints on $|\Delta m|$ distributions, which is the difference between the invariant mass calculated with information from daughter tracks, and the known, tabulated invariant mass of a particle; it is, thus, defined as $|\Delta m| = m_{\text{calculated}} - m_{\text{tabulated}}$. The $|\Delta m|$ distributions will have a peak around 0, for "correct" candidates.

- **$|\Delta m|$ around nominal Λ mass ($|\Delta m_{\Lambda}|$):** background was reduced with this cut, which only accepted Λ candidates with a calculated mass similar to the known Λ mass.

- **$|\Delta m|$ around nominal Ξ mass ($|\Delta m_{\Xi}|$):** in figure 9 the invariant mass distribution of Ξ versus the invariant mass distribution of Ω is shown. As can be seen in the figure, the number of Ξ candidates exceeds the number of Ω candidates and thus in their overlapping area (approximately the center of the histogram) there is a much larger likelihood that the candidates are Ξ particles. For this reason, all Ω candidates whose invariant mass was compatible with the Ξ mass were rejected; in the figure this is the area within the black lines.

- **Rapidity (y):** the cut on rapidity, which was applied for Ω, is similar to the pseudorapidity cut applied in order to reject the tracks which do not have full detector acceptance. In Figure 10a and 10b the rapidity distributions for Ω^- and Ω^+, respectively, are shown both for real data and MC data. As can be seen in the figure, the rapidity, and thus the acceptance, starts decreasing already at $|y| \sim 0.5$, which is towards the edges of the detector.

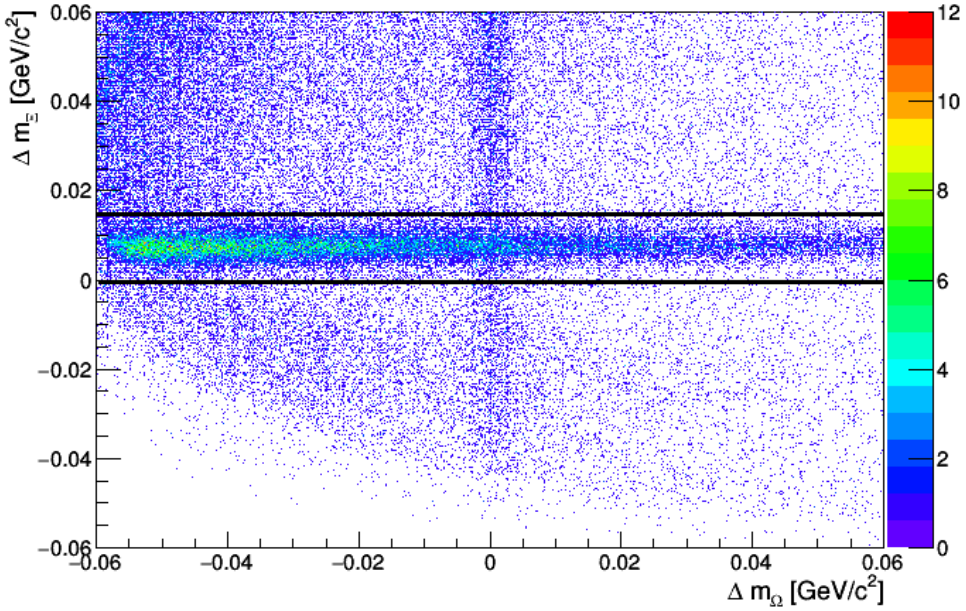

Figure 9: The Ξ invariant mass distribution as a function of the Ω invariant mass distribution. At approximately the center of the histogram, the Ξ and Ω candidates coincide.

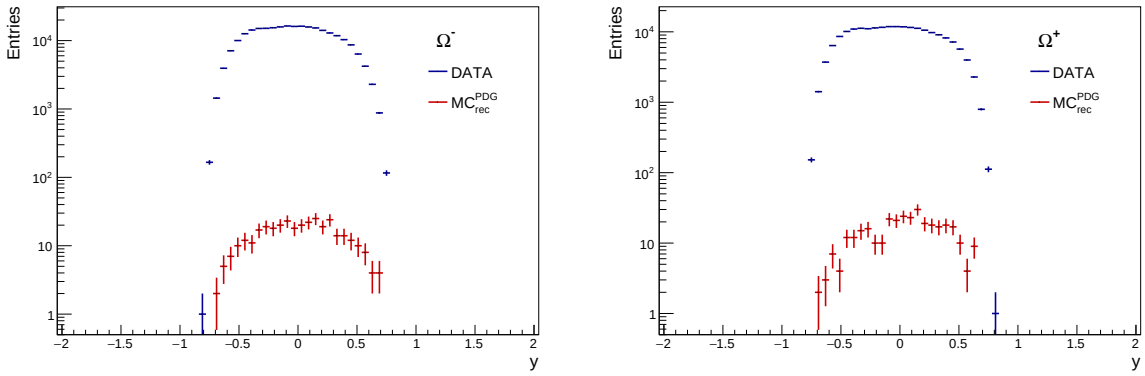

(a) The Ω^- rapidity.

(b) The Ω^+ rapidity.

Figure 10: The Ω rapidity, for both experimental data and MC data.

Table 4: Selection criteria applied for the p, π, Λ, K and Ω candidates. The tracks needed to fulfil the following criteria in order to not be discarded.

V^0 daughter track selection	
Pseudorapidity	$\lvert\eta\rvert < 0.8$
TPC PID	$N_\sigma < 4$
DCA of V^0 daughter track to PV	$DCA_{V^0\text{daughters-PV}} > 0.03$ cm
V^0 selection	
DCA between V^0 daughter tracks	$DCA_{V^0\text{daughters}} < 1.5$ cm
Transverse decay radius	$r_{dec} > 1.4$ cm
Cosine of pointing angle	cos(PA)> 0.97
$\lvert\Delta m\rvert$ around nominal Λ mass	$\lvert\Delta m_\Lambda\rvert < 6$ MeV/c^2
Bachelor track selection	
Pseudorapidity	$\lvert\eta\rvert < 0.8$
TPC PID	$N_\sigma < 4$
DCA of bachelor track to PV	$DCA_{\text{Bachelor-PV}} > 0.05$ cm
Cascade selection	
DCA between V^0 and bachelor track	$DCA_{\text{Bachelor-}V^0} < 1$ cm
Transverse decay radius	$r_{dec} > 0.6$ cm
Cosine of pointing angle	cos(PA)> 0.97
$\lvert\Delta m\rvert$ around nominal Ξ mass	$\Delta m_\Xi < 0$ MeV/c^2
	$\Delta m_\Xi > 15$ MeV/c^2
Rapidity	$\lvert y\rvert < 0.5$

5.4 Signal Extraction

When all the selection cuts were applied, two-dimensional histograms were made with the invariant mass distributions of Ω as a function of p_T. This was done for real data, for $\mathrm{MC}_{rec}^{blind}$ data, and for MC_{rec}^{PDG} data. As was previously mentioned, the analysis with $\mathrm{MC}_{rec}^{blind}$ data, was performed in exactly the same way as with real data, while the analysis with MC_{rec}^{PDG} data selects only the correct Ω candidates (after applying the "normal" selection cuts). Figures 11, 12, and 13 show the histograms of the invariant mass distributions as functions of p_T for real, $\mathrm{MC}_{rec}^{blind}$, and MC_{rec}^{PDG} data, respectively, with Ω^- in figure (a) and Ω^+ in figure (b).

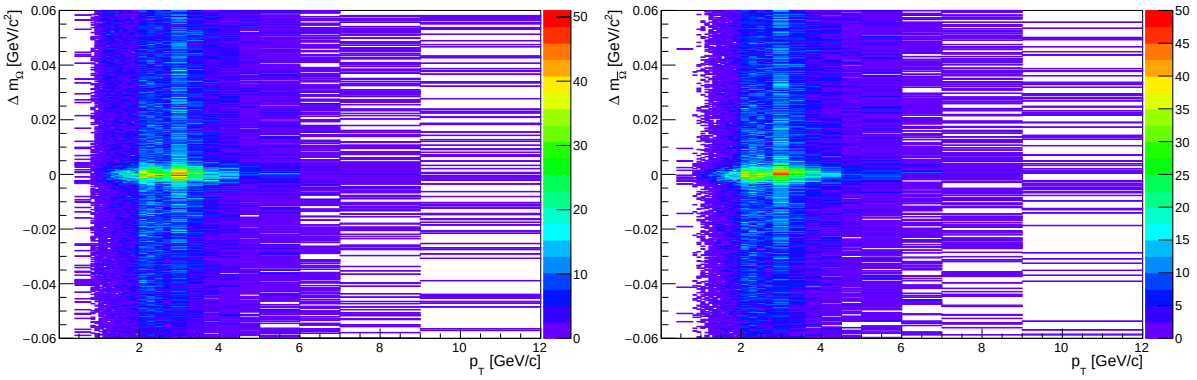

(a) Ω^- (b) Ω^+

Figure 11: The Δm_Ω distribution as a function of p_T for experimental data.

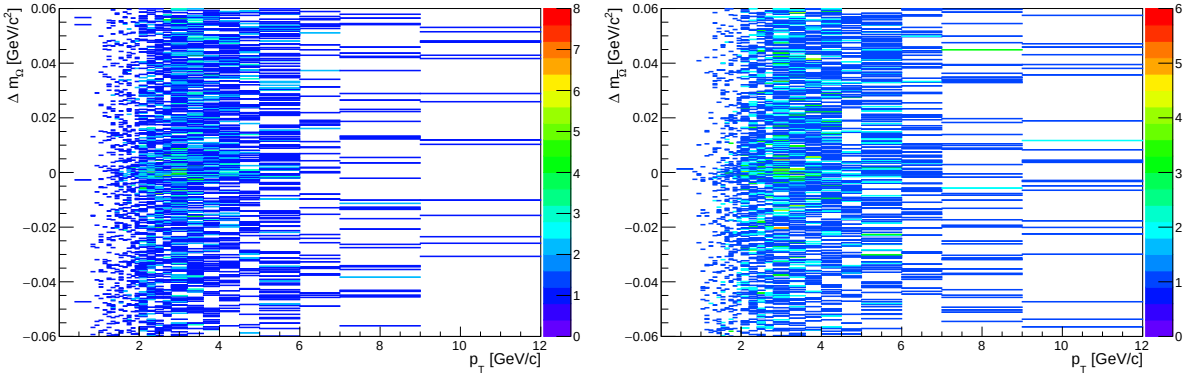

(a) Ω^- (b) Ω^+

Figure 12: The Δm_Ω distribution as a function of p_T for $\mathrm{MC}_{rec}^{blind}$ data.

The Ω signal around 0 in the mass distribution, and the background, can clearly be seen in figure 11. However, in figure 12 no such signal can be seen. This can be explained by the known fact that in MC data the production of strange particles is restrained [22]. The more strange quarks a hadron is composed of, the more suppressed its production is

in MC data. When using the MC_{rec}^{PDG} data, the signal in the distribution can once again be seen, as the background is removed when selecting the correct Ω candidates.

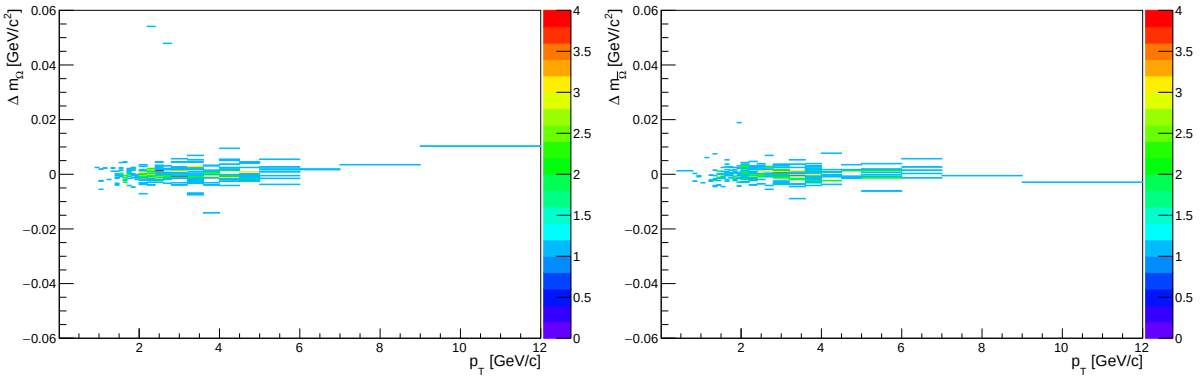

(a) Ω^- (b) Ω^+

Figure 13: The Δm_Ω distribution as a function of p_T for MC_{rec}^{PDG} data.

From the histograms in figure 11 and figure 13 the visible signal was extracted. Projections to the y-axis in each p_T bin were made, giving one-dimensional histograms of the invariant mass distributions within a certain p_T range. For real data, the Ω yield was extracted, for each p_T bin, from these one-dimensional invariant mass distributions by the sideband subtraction method (which will be explained below), however, for the MC_{rec}^{PDG} this was not necessary, as the background had already been removed.

5.4.1 The Sideband Subtraction Method

In figure 14 the one-dimensional invariant mass distributions, obtained from figure 11, are shown for the experimental data, in the p_T range $1.80 - 2.80$ GeV/c. The sideband subtraction method can be applied by defining the peak region, assuming a linear background, and defining two "sidebands". The sidebands are on each side of the peak, as in figure 14, and the sum of their widths is equal to the width of the peak region. The peak region was defined by following the analysis in reference [8], and to ensure that the risk of removing part of the signal is minimal, chosen to be within the range -0.008 $< \Delta m <$ 0.008 GeV/c^2, while the sidebands were defined to be in the ranges -0.016 $< \Delta m <$ -0.008 GeV/c^2 and 0.008 $< \Delta m <$ 0.016 GeV/c^2. What the sideband subtraction method then assumes, when assuming a linear background, is that the background in the peak region is equal to the sum of the background in the sidebands. Thus, the background in the peak region can be removed by subtracting the background of the sidebands regions from the peak region. Thus, the signal S, in each p_T bin, can be extracted by:

$$S = N_{\text{Signal}} - N_{\text{Sidebands}}. \tag{14}$$

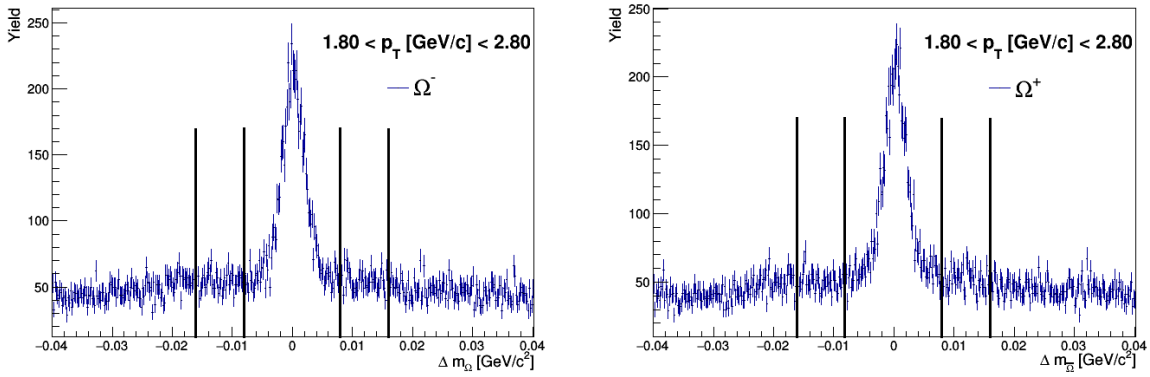

(a) Ω^- (b) Ω^+

Figure 14: The Δm_Ω distribution for experimental data in the p_T range $1.80 - 2.80$ GeV/c.

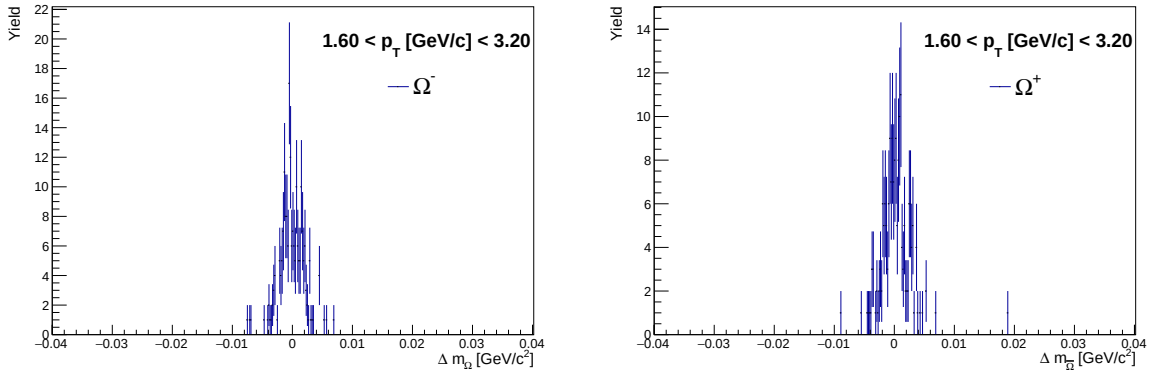

(a) Ω^- (b) Ω^+

Figure 15: The Δm_Ω distribution for MC_{rec}^{PDG} data in the p_T range $1.60 - 3.20$ GeV/c.

In figure 15 the invariant mass distributions, obtained from figure 13, are shown for the MC_{rec}^{PDG} data, in the p_T range $1.60 - 3.20$ GeV/c. The reason for the larger p_T-interval (compared to the p_T interval of figure 14) is the lower amount of statistics, due to the previously mentioned smaller amount of events in the MC data sample, and the reduced number of strange hadrons in MC data. As can be seen in the figure, there is no background to subtract, and the signal in each bin can be extracted directly from these histograms, without applying the sideband subtraction method.

5.5 The Transverse Momentum Spectra

Once the four signals S (for the different data sets and for Ω^- and Ω^+) in all p_T bins were extracted, they were normalized to the number of accepted events (N_{ev} for experimental data and $N_{\text{ev}}^{\text{MC}}$ for MC data, both given in section 5.3), to the rapidity window (dy, where $|y| < 0.5$), and to the p_T bin widths (dp_T). This gave the uncorrected, but normalized, Ω yields Y_{uncorr}:

$$Y_{\text{uncorr}} = \frac{S}{N_{\text{ev}}} \times \frac{1}{\Delta p_T} \times \frac{1}{\Delta y} = \frac{1}{N_{\text{ev}}} \frac{\mathrm{d}^2 N}{\mathrm{d}p_T \mathrm{d}y} \tag{15}$$

With these yields, four different p_T-spectra were made, where the Ω yields were expressed as functions of p_T. These uncorrected, but normalized, p_T spectra are shown in figure 16a for Ω^- and 16b for Ω^+; the figures show the spectra for both experimental data and MC_{rec}^{PDG} data. As expected, the amount of strangeness is not at all reproduced by the simulated data.

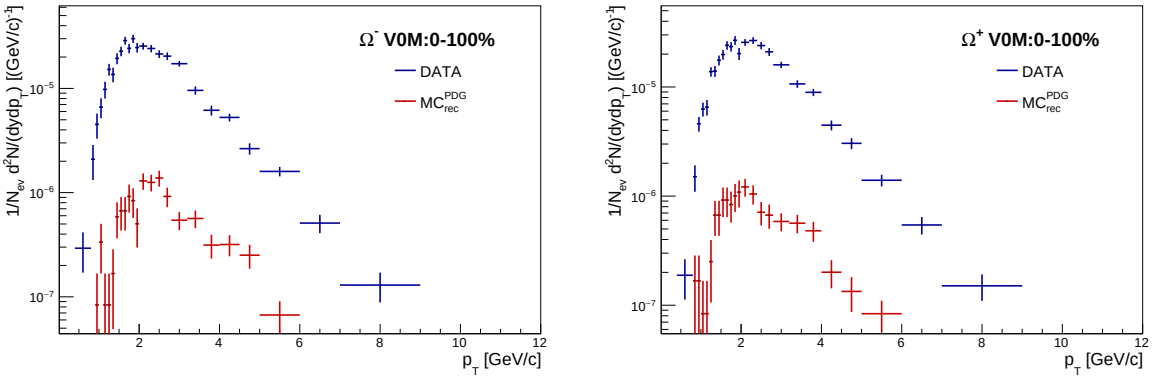

(a) Uncorrected p_T-spectra for Ω^-.

(b) Uncorrected p_T-spectra for Ω^+.

Figure 16: Uncorrected p_T-spectra for experimental and simulated data.

5.5.1 Efficiency Corrections

In addition to being normalized, the p_T-spectra have to be corrected in order to account for the imperfections of the detector and the analysis. This can be done by calculating the efficiency, as this corrects for acceptance limitations and for reconstruction efficiency. The acceptance (Acc) corrects for detector coverage, i.e. for the fraction of signal events that are not visible to the detector, while the reconstruction efficiency (Eff_{rec}) corrects for the fraction of wrongly discarded events in the reconstruction and identification of the Ω candidates. The full efficiency is, thus, calculated as:

$$\text{Efficiency} = \text{Acc} \times \text{Eff}_{rec} = \frac{\text{MC}_{rec}^{PDG}}{\text{MC}_{gen}} \tag{16}$$

where MC_{gen} are all the MC generated Ω:s, before passing through the detector and reconstruction simulation. The efficiency, as a function of p_T, for the Ω baryon can be

seen in figure 17.

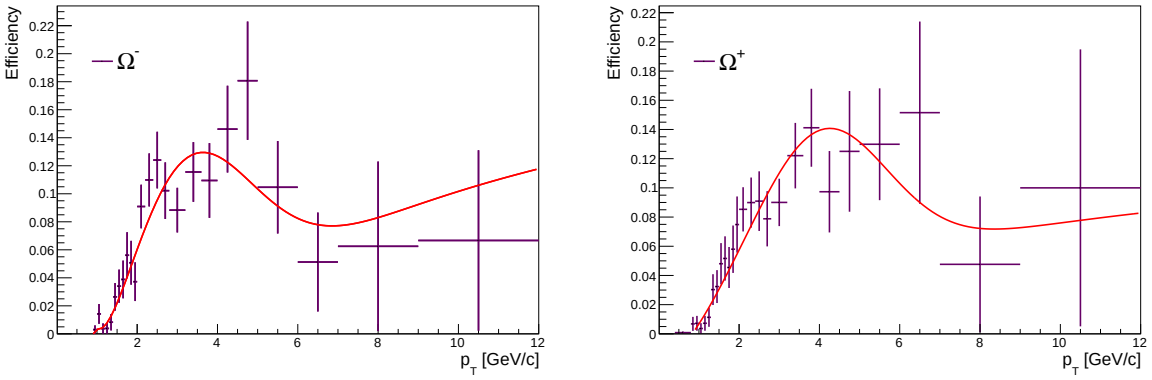

(a) The calculated efficiency for Ω^- (b) The calculated efficiency for Ω^+

Figure 17: The calculated efficiency, which is used to correct the particle yield for the acceptance limitations in the detector and the reconstruction limitations, as a function of p_T.

The histograms in figure 17 have been fitted with the function

$$f_{fit} = [a] \cdot \exp\left(-\frac{(x-[b])^2}{[c]^2}\right) + [d] \cdot \log(x^{1/2} - [f]) \cdot (1 - \exp([g] - x)), \tag{17}$$

where the letters in square brackets are parameters. The function was used in the analysis of reference [21]; it was experimentally determined and does not have any particular physical motivation. This fit function was then used to correct the yield Y_{uncorr}, giving the corrected yield Y_{corr}:

$$Y_{corr} = \frac{S}{N_{\text{ev}}} \times \frac{1}{\Delta p_T} \times \frac{1}{\Delta y} \times \frac{1}{\text{Efficiency}} = \frac{1}{N_{\text{ev}}} \frac{\mathrm{d}^2 N}{\mathrm{d}p_T \mathrm{d}y} \tag{18}$$

From hereon, the p_T-spectra shown will be corrected spectra.

5.6 Multiplicity Dependence of Production

The aim of this analysis was to analyze the production of Ω baryons as a function of multiplicity. In order to do this, the events analyzed had to be separated into different multiplicity classes, namely:

- V0M: 0 – 10%, i.e. of all the events, the 10% events with highest multiplicities
- V0M: 10 – 50%, i.e. of all the events, the 40% events with intermediate multiplicities
- V0M: 50 – 100% i.e. of all the events, the 50% events with lowest multiplicities

where V0M stands for V0 multiplicity, which is the multiplicity measured by the V0 (or VZERO) detector, described in section 3.1.3. The V0 detector is included in the forward detectors and thus, covers the forward regions, i.e. measures the multiplicity at small angles with respect to the beam axis. A "selection" of V0M: 0 – 100 % will indicate no V0M selection, thus all events are included.

By choosing the events with highest multiplicities, the events where most charged particles are created are being chosen, thus having a larger yield of strange particles could be due to more particles being created in general. To make an additional comparison with the strange particle yields, the number of charged particles N_{ch}, measured by the central-barrel detectors in the mid-rapidity region (instead of the multiplicity in the forward region) was used. Three distributions of the number of charged particles are shown in figure 18, separated by the V0M multiplicity classes.

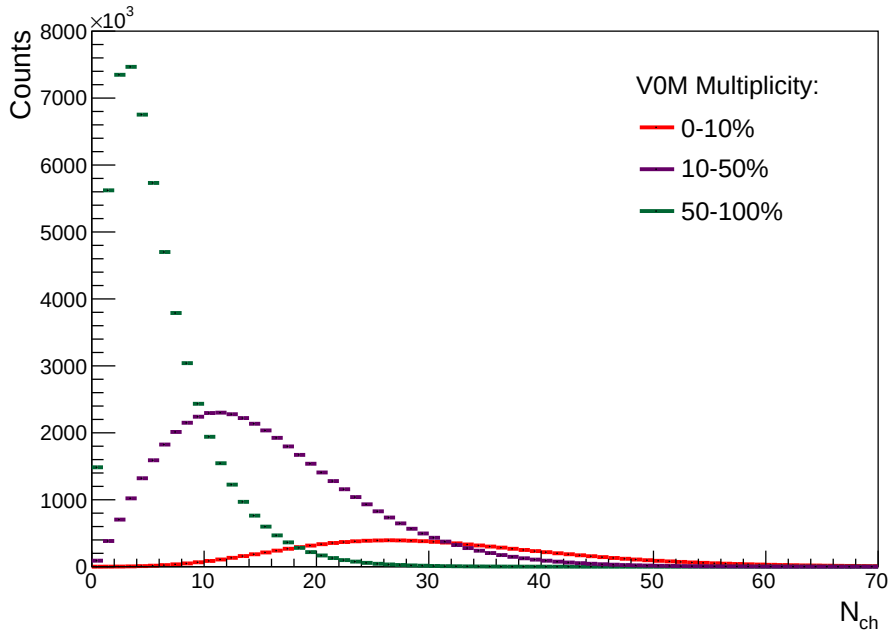

Figure 18: The three different N_{ch} distributions, separated by the V0M multiplicity classes.

For this additional cross-check, the three corrected p_T spectra obtained for the different multiplicty classes (shown in the next section), were integrated, giving the total Ω yields. The yields for the Ω^- (N^-_Ω) and Ω^+ (N^+_Ω), in each V0M class, were added and then divided by the mean value of N_{ch} in the respective distribution. Finally, this ratio was expressed as a function of N_{ch}.

6 Results & Discussion

Figures 19a and 19b show the Ω^- and the Ω^+ baryon production, in proton-proton collisions at $\sqrt{s} = 13$ TeV, as a function of p_T. No major difference can be seen between the particle and antiparticle production. Both figures show four histograms each, one being event multiplicity unbiased (V0M:0-100%) and three corresponding to the three different event multiplicity selections (V0M:0-10%, 10-50%, 50-100%). Above ~ 1 GeV/c the two figures clearly show the event multiplicity dependence of the production of the baryons and the enhancement of the production as the event multiplicity increases. This enhancement appears to increase with p_T, although, at $p_T \gtrsim 5$ GeV/c the statistics decreases significantly, as could already be seen in figure 11. The statistics also decreases when the $p_T \lesssim 1$ GeV/c. Furthermore, the p_T-spectra for unbiased multiplicity events and for the intermediate multiplicity events (V0M:10-50%) are similar. This multiplicity dependence of the production of the multi-strange Ω in pp-collisions has previously been observed in reference [22], as was mentioned in section 4.2. The results, from reference [22], shown in figure 6a seem to be in reasonable agreement with the results shown in figure 19.

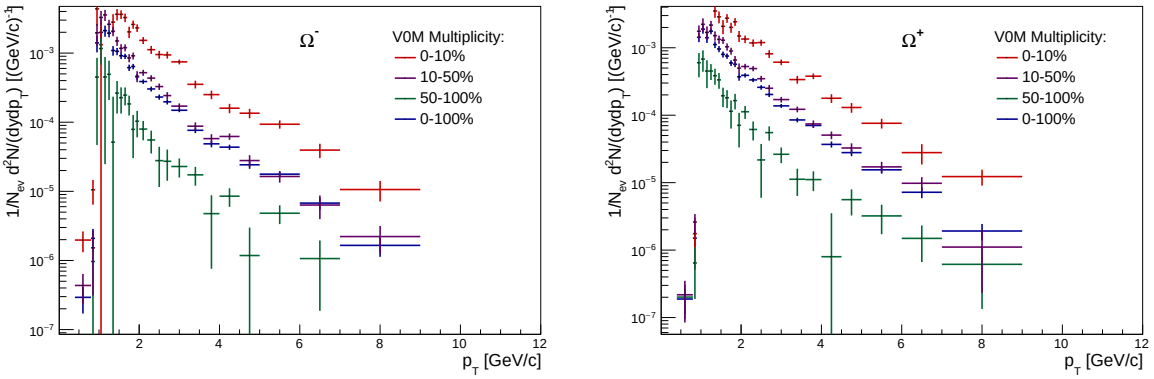

(a) The p_T-spectra for the Ω^- baryon.

(b) The p_T-spectra for the Ω^+ baryon.

Figure 19: The figures show four different (corrected) p_T-spectra each: one for multiplicity unbiased events and three for the three different multiplicity selections, V0M:0-10%, 10-50%, and 50-100%.

Figure 20 then shows the ratio of the p_T integrated Ω yield ($\Omega^- + \Omega^+$) to the mean value of the N_{ch} distribution, in the respective V0M classes, as a function of N_{ch} – which is the additional cross-check performed to analyze the increase of the Ω baryon production. As can be seen in the figure, Ω/N_{ch} increases with N_{ch}. The value of the ratio is nearly twice as high for the highest multiplicity class, compared to the lowest. This result can not as easily be compared to the result shown in figure 6b, from reference [22], since the variables are not quite the same. However, it can clearly be seen that both the ratios (in figure 6b and in figure 20) increase significantly with multiplicity, while the ratios found here are likely somewhat lower. To conclude more firmly on this, further analysis and

cross-checks are needed as discussed in the next section.

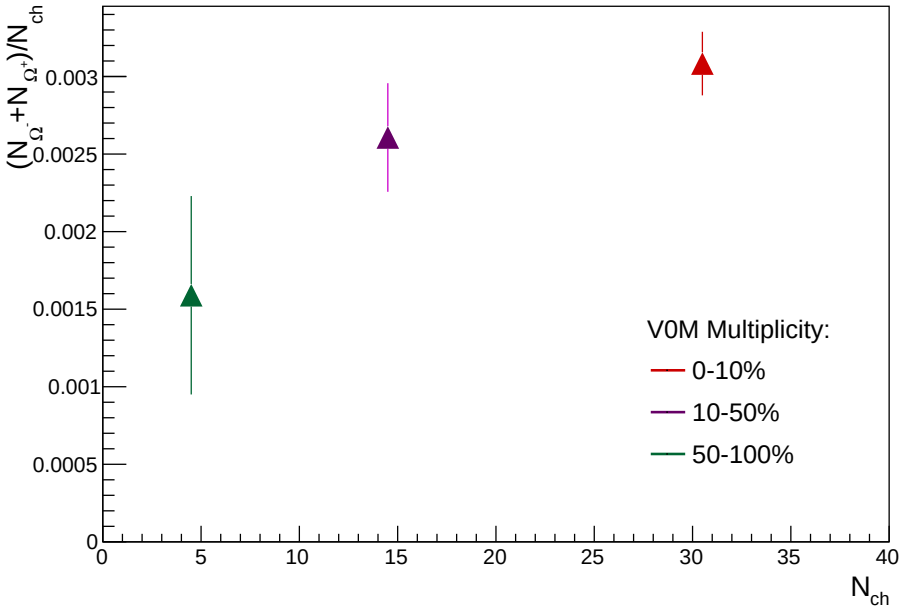

Figure 20: Ratio of p_T integrated Ω yield ($\Omega^- + \Omega^+$) to the mean value of the N_{ch} distribution, in the respective V0M class, as a function of N_{ch}.

7 Conclusion & Outlook

In this thesis the production of the Ω^- and Ω^+ baryons as a function of multiplicity, in proton-proton collisions at $\sqrt{s} = 13$ TeV, was analyzed. The events analyzed were separated according to their event multiplicity and the baryon candidates were reconstructed, through their cascade decay topology, and identified, through several selection criteria. The results obtained clearly show the dependence on event charged-particle multiplicity of the production, and that higher-multiplicity events have an enhanced production of Ω baryons – agreeing with previous studies. Although, in order to examine the validity of the results obtained in this analysis, the systematic uncertainties would have to be studied further.

The results from this analysis could be improved in various ways. When selecting the Ω candidates, the selection criteria chosen had been used in the analysis described in reference [28]. The selection criteria were tested but not confirmed as optimal in this analysis; if the selection criteria had primarily been tested on MC data, the selection criteria could have been improved in order to minimize the background (further), while keeping the "correct" candidates. Furthermore, the signal extraction could also have been improved. This could have been done by selecting the peak-region, and the sidebands, in each p_T bin instead of fixing the peak-region to the chosen value. Finally, the function chosen to fit the acceptance-efficiency distribution, shown in figure 17, was taken from

the analysis performed in reference [21]. This fit function, although reasonable at $p_T \leq 4$ GeV/c – where most of the particle yield is – does not seem to fit the efficiency curvature at larger p_T.

The study described in reference [22], introduced in section 4.2, to which this analysis is briefly compared, analyses not only the production of the Ω baryon, but also that of the Ξ, Λ, and K_s^0 hadrons. In order to thoroughly study the strangeness enhancement at high multiplicities, comparisons between different analyses should be made, which is why the production of the other hadrons is presently being analyzed.

A natural continuation for this analysis would be to study the production of the Ω baryon as a function of transverse spherocity, an event shape estimator which measures the geometrical distribution of the p_T and separates the collisions according to that. When QGP is created in heavy ion collisions, the transverse spherocity $\rightarrow 1$, thus analysing the Ω production in pp collisions, as a function of multiplicity and spherocity could give more clues to whether QGP is or is not created in small collisional systems.

References

[1] Kane GL. MODERN ELEMENTARY PARTICLE PHYSICS. Cambridge University Press; 2017. Available from: http://www.cambridge.org/academic/subjects/physics/particle-physics-and-nuclear-physics/modern-elementary-particle-physics-explaining-and-extending-standard-model-2nd-edition?format=ARisbn=9781316730805.

[2] Martin BR, Shaw G. Particle physics; 4th ed. Manchester physics series. New York, NY: Wiley; 2017. Available from: http://cds.cern.ch/record/2211679.

[3] Griffiths D. Introduction to elementary particles; 2008.

[4] Thomson M. Modern particle physics. New York: Cambridge University Press; 2013. Available from: http://www-spires.fnal.gov/spires/find/books/www?cl=QC793.2.T46::2013.

[5] Chaudhuri AK. A short course on Relativistic Heavy Ion Collisions. IOPP; 2014.

[6] The Large Hadron Collider;. Accessed: 2019-04-28. https://home.cern/science/accelerators/large-hadron-collider.

[7] Facts and Figures About the LHC;. Accessed: 2019-04-28. https://home.cern/resources/faqs/facts-and-figures-about-lhc.

[8] Mårtenson M. Strange Hadron Production as a Function of Multiplicity and Transverse Spherocity in proton-proton Collisions at $\sqrt{s} = 13$ TeV; 2018. Student Paper.

[9] ALICE;. Accessed: 2019-04-28. http://alice.web.cern.ch.

[10] Betev L, Chochula P. Definition of the ALICE Coordinate System and Basic Rules for Subdetector Components Numbering. 2003;.

[11] Abelev BB, et al. Performance of the ALICE Experiment at the CERN LHC. Int J Mod Phys. 2014;A29:1430044.

[12] Aamodt K, et al. The ALICE experiment at the CERN LHC. JINST. 2008;3:S08002.

[13] Alme J, et al. The ALICE TPC, a large 3-dimensional tracking device with fast readout for ultra-high multiplicity events. Nucl Instrum Meth. 2010;A622:316–367.

[14] More details on the ALICE TPC;. Accessed: 2019-04-28. http://alice.web.cern.ch/detectors/more-details-alice-tpc.

[15] Richert TOH. Λ/K^0_s associated with a jet in central Pb-Pb collisions at $\sqrt{s_{NN}} = 2.76$ TeV measured with the ALICE detector. Lund U.; 2016-05-16.

[16] Aamodt K, et al. Centrality dependence of the charged-particle multiplicity density at mid-rapidity in Pb-Pb collisions at $\sqrt{s_{NN}} = 2.76$ TeV. Phys Rev Lett. 2011;106:032301.

[17] Jönsson L. Lectures in Particle Physics;. Latest update 2015.

[18] Barr G, Devenish R, Walczak R, Weidberg T. Particle physics in the LHC era. Oxford master series in particle physics, astrophysics and cosmology. Oxford: Oxford University Press; 2016. Available from: https://cds.cern.ch/record/2034442.

[19] Bakhet N, Khlopov MYu, Hussein T. Neural Networks Search for Charged Higgs Boson of Two Doublet Higgs Model at the Hadrons Colliders. 2015;.

[20] Braun-Munzinger P, Stachel J. The quest for the quark-gluon plasma. Nature. 2007;448:302–309.

[21] Colella D, Elia D. Measurements of multi-strange baryons in pp collisions at $\sqrt{s} =$ 13 TeV. 2016;Analysis note submitted for publication.

[22] Adam J, et al. Enhanced production of multi-strange hadrons in high-multiplicity proton-proton collisions. Nature Phys. 2017;13:535–539.

[23] ALICE Offline;. Accessed: 2019-04-20. http://alice-offline.web.cern.ch.

[24] Antcheva I, et al. ROOT: A C++ framework for petabyte data storage, statistical analysis and visualization. Comput Phys Commun. 2009;180:2499–2512.

[25] Sjostrand T, Mrenna S, Skands PZ. PYTHIA 6.4 Physics and Manual. JHEP. 2006;05:026.

[26] Agostinelli S, et al. GEANT4: A Simulation toolkit. Nucl Instrum Meth. 2003;A506:250–303.

[27] Tanabashi M, et al. Review of Particle Physics. Phys Rev. 2018;D98(3):030001.

[28] Production of light flavor hadrons in pp collisions at $\sqrt{s} = 7$ TeV and $\sqrt{s} = 13$ TeV. 2019;Article submitted for publication.

[29] Angelsmark M. Xi Production in pp Collisions with Different Multiplicity and Sphericity; 2019. Student Paper.